analytical chemistry

pubs.acs.org/ac Article

Plasmonic Colorimetric Biosensor for Sensitive Exosome Detection via Enzyme-Induced Etching of Gold Nanobipyramid@MnO_2 Nanosheet Nanostructures

Yingzhi Zhang, Junye Jiao, Yunyun Wei, Danni Wang, Chunguang Yang,* and Zhangrun Xu*

Cite This: https://dx.doi.org/10.1021/acs.analchem.0c04136 Read Online

ACCESS | Metrics & More | Article Recommendations | Supporting Information

ABSTRACT: Exosomes involved in tumor-specific processes display excellent potential in the early diagnosis of cancer. Herein, a highly sensitive plasmonic colorimetric biosensor was proposed for exosome quantification. The sensing strategy mainly includes two steps: exosome-triggered competitive reaction and etching of gold nanobipyramid@MnO_2 nanosheet nanostructures (Au NBP@MnO_2 NSs). A competitive reaction between exosomes and placeholder chains induced by exosomes can translate the signal of exosomes into the amount of alkaline phosphatase, which simplifies the experimental process and amplifies the signal. The etching of Au NBP@MnO_2 NSs by ascorbic acid generated from the hydrolysis of L-ascorbic acid 2-phosphate by alkaline phosphatase changes the refractive index of Au NBPs, accompanied by the blue shift of the longitudinal localized surface plasmon resonance peak. Profiting from the signal amplification of the competitive reaction and superior refractive index sensitivity of colorimetric substrates, this protocol exhibits high sensitivity toward exosomes within 8.5×10^2 to 8.5×10^4 particles μL^{-1}, along with a detection limit of 1.35×10^2 particles μL^{-1}, which is more sensitive than previously reported colorimetric methods. In addition, a sensitive multicolor visual detection of exosomes was realized by adjusting the aspect ratio of Au NBPs. It is worth mentioning that the Au NBP@MnO_2 NSs was synthesized through in situ growth of MnO_2 nanosheets on Au NBPs, and the attractive optical properties and ease of etching make Au NBP@MnO_2 NSs promising candidates for plasmonic detection.

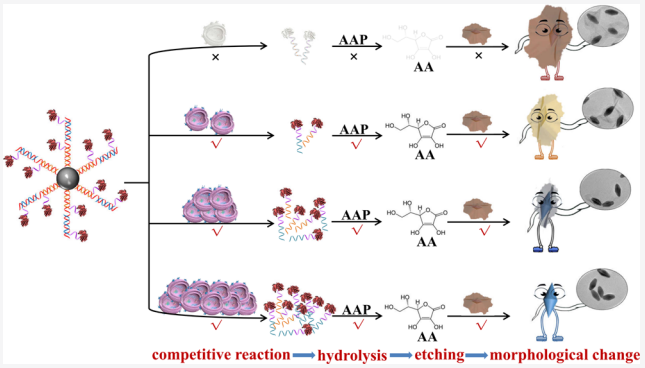

INTRODUCTION

Exosomes, nanoscale membrane-encapsulated vesicles, are secreted by living cells into the extracellular environment and widely exist in various body fluids.[1−3] Previous studies have indicated that exosomes derived from cancer cells consist of plentiful tumor-specific substances (e.g., proteins, nucleic acids, and bioactive lipids) and display remarkable molecular heterogeneity owing to different origins. The concentrations of exosomes are significantly upregulated in the body fluids of cancer patients compared to those in healthy people.[4−6] In addition, exosomes derived from cancer cells are closely related to tumor-specific processes, including occurrence, proliferation, and metastasis of tumors.[7−9] Therefore, exosomes can be used as a noninvasive tumor marker for cancer diagnosis, prognosis, and treatment monitoring.

Over the past few years, numerous strategies have been developed for sensitive detection of exosomes, such as electrochemistry,[10,11] fluorescence,[12,13] colorimetry,[14,15] and surface-enhanced Raman scattering (SERS).[16,17] In addition, single-exosome identification has been explored using the SERS method.[18] Although these methods greatly promote the development of exosome detection, the requirement of relatively professional operation and delicate instruments limits their application. Among the methods, colorimetry exhibits attractive potential in naked-eye quantification and portability. Some traditional colorimetric methods have been proposed for exosome detection.[14,15,19,20] These methods usually employ organic chromogens, 2,2′-azinobis-(3-ethylbenzthiazoline-6-sulphonate) (ABTS) or 3,3′,5,5′-tetramethyl benzidine (TMB), as a colorimetric substrate, and their sensitivity is often limited because the extinction coefficients of the organic chromogens are undesirable. Furthermore, these strategies basically depend on the alteration of optical density of one color, yet our eyes are insensitive to optical density variation. There are two ways to overcome the abovementioned limitations: one is to integrate signal amplification strategies

Received: October 1, 2020
Accepted: October 14, 2020

Scheme 1. Schematic of the Fabrication Process of Au NBP@MnO_2 NSs

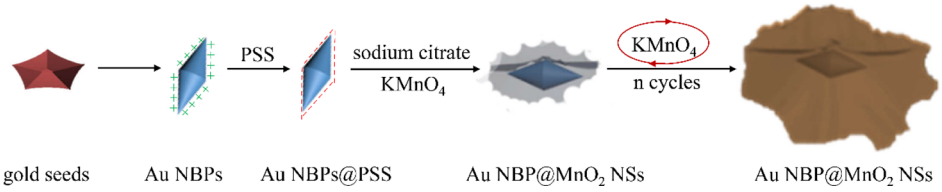

and the other is to improve the performance of colorimetric substrates.[21−24]

Compared with the traditional colorimetric assays, plasmon-based colorimetric sensing presents more fascinating virtues, such as enhanced sensitivity and plentiful color variation, owing to the superiority of plasmonic colorimetric substrates.[25] According to signal formation principles, the plasmonic colorimetric sensing can be divided into two categories: plasmonic nanoparticle aggregation-based colorimetric assay and plasmonic nanoparticle etching/growth-based colorimetric assay. The former depends on the target-triggered change of the interparticle distance. However, the plasmonic nanoparticle aggregation is influenced by various external factors, which easily leads to boresome interference. The latter relies on the morphology change of nanoparticles caused by target-induced etching/growth.[26−29] We recently reported a plasmonic colorimetric method for exosome detection via enzyme-induced silver growth on gold nanorods (Au NRs) and hybridization chain reaction (HCR).[30] This method realized the sensitive multicolor visual detection of exosomes for the first time, whereas the detection procedure is tedious. Both Au NRs and Au NBPs can serve as substrates for plasmonic detection. The rounded-end shape of Au NRs makes the localized surface plasmon resonance (LSPR) bands broaden inhomogeneously, which limits their refractive index sensitivity.[31,32] Unlike Au NRs and other plasmonic noble metal structures, Au NBPs own two pentagonal pyramids with sharper tips at their apexes, which makes them more sensitive to the refractive index.[33−35] For example, Guo's group proposed a colorimetric strategy for influenza virus detection based on metallization of Au NBPs instead of Au NRs and the Au NBP-based method is more sensitive.[36] Therefore, Au NBPs with remarkable optical properties are accounted as ideal candidates for plasmonic colorimetric sensing.

In this work, we aim to develop a sensitive and easy-to-operate plasmonic colorimetric strategy for exosome detection. Toward this goal, efforts were made to improve the performance of colorimetric substrates and simplify the experimental process. The procedure only consists of two parts. In the first part, exosomes initiate competitive reaction, during which a mass of alkaline phosphatases (ALPs) are produced via the design of multiple placeholder chains, effectively simplifying the process and amplifying the signal. In the second part, Au NBP@MnO_2 NSs are rationally designed as etching substrates. The expected merits of the substrates are as follows. First, Au NBPs possess enhanced sensitivity in plasmonic sensing compared with other plasmonic noble metal structures, which ensures the favorable sensitivity for exosome assay. Second, Au NBPs are modified with poly(4-styrenesulfonic acid) (PSS) during the synthesis process, which will increase the colloidal stability of the substrates. Third, the Au NBP@MnO_2 NSs are easier to be etched by reductants compared with the previously reported plasmonic nanoparticles, which usually are etched using strong oxidants as etchants. By means of the abovementioned virtues of the substrates, exosomes can be simply and sensitively detected using the proposed plasmonic colorimetric strategy.

EXPERIMENTAL SECTION

Synthesis of Au NBPs and Au NBP@MnO_2 NSs. The Au NBPs were synthesized according to the seed-mediated growth method (Supporting Information).[37] Inspired by the previously reported work,[38] we designed a novel plasmonic probe consisting of Au NBPs and MnO_2 nanosheets. Au NBP@MnO_2 NSs were fabricated through in situ growth of MnO_2 nanosheets on Au NBPs, and the specific processes are as follows (Scheme 1). (1) A total of 20 mL of as-purified Au NBPs was dispersed in 20 mL of 4 g L^{-1} PSS solution (containing 6 mM NaCl), and the solution was stirred for 30 min at room temperature. Then, excess cetyltrimethylammonium chloride (CTAC) and PSS were removed by centrifuging twice at 6000 rpm for 20 min. The modification of PSS is to alter the electrical property and improve the stability of Au NBPs. The zeta potentials of Au NBPs and Au NBPs@PSS were measured by dynamic light scattering (DLS, Nano ZS90, Malvern, England). (2) The obtained Au NBPs@PSS was dissolved in 20 mL of 5 mM sodium citrate solution. Then, 0.2 mL of 10 mM $KMnO_4$ was added into the abovementioned solution dropwise under efficient stirring. The mixture was heated for 4 h at 35 °C under static conditions, resulting in the in situ growth of MnO_2 nanosheets on Au NBPs. The abovementioned processes were repeated several times to obtain needed Au NBP@MnO_2 NSs. The obtained solution was centrifuged at 6000 rpm for 10 min three times, and the final precipitate was redispersed in ultrapure water. The extinction spectra of Au NBPs, Au NBPs@PSS, and Au NBP@MnO_2 NSs were measured using a UV−vis spectrophotometer (TU-1901, Persee, Beijing, China). The morphologies of Au NBPs, Au NBPs@PSS, and Au NBP@MnO_2 NSs were observed using a transmission electron microscope with an accelerating voltage of 200 kV (FEI Tecnai G2, F20 and JEM2100 PLUS).

Modification of Aptamers on Magnetic Beads. Biotinylated CD63 aptamers and streptavidin-functionalized magnetic beads (1 μm in diameter) were conjugated as follows. First, 100 μL of 10 mg mL^{-1} magnetic beads was washed three times using phosphate-buffered saline (PBS, containing 0.05% Tween 20, pH 7.4) and resuspended in 1 mL of 1 μM CD63 aptamer, followed by rolling for 1 h. Excess CD63 aptamers were removed by magnetic separation, and the magnetic bead/CD63 aptamer was washed three times with PBS buffer. Then, two placeholder chains, partially complementary with the CD63 aptamer, were introduced for competitive reaction. A total of 0.5 mL of 2 μM placeholder chain 1 labeled with ALP (P1-ALP) and 0.5 mL of 2 μM placeholder chain 2 labeled with ALP (P2-ALP) were added to redisperse the magnetic bead/CD63 aptamer, and the mixture solution was incubated at 37 °C for 1 h. Finally, excess P1-ALP and P2-ALP were

https://dx.doi.org/10.1021/acs.analchem.0c04136
Anal. Chem. XXXX, XXX, XXX−XXX

Scheme 2. Schematic Illustration of the Plasmonic Colorimetry for Exosome Detection via Competitive Reaction and Etching of Au NBP@MnO_2 NSs

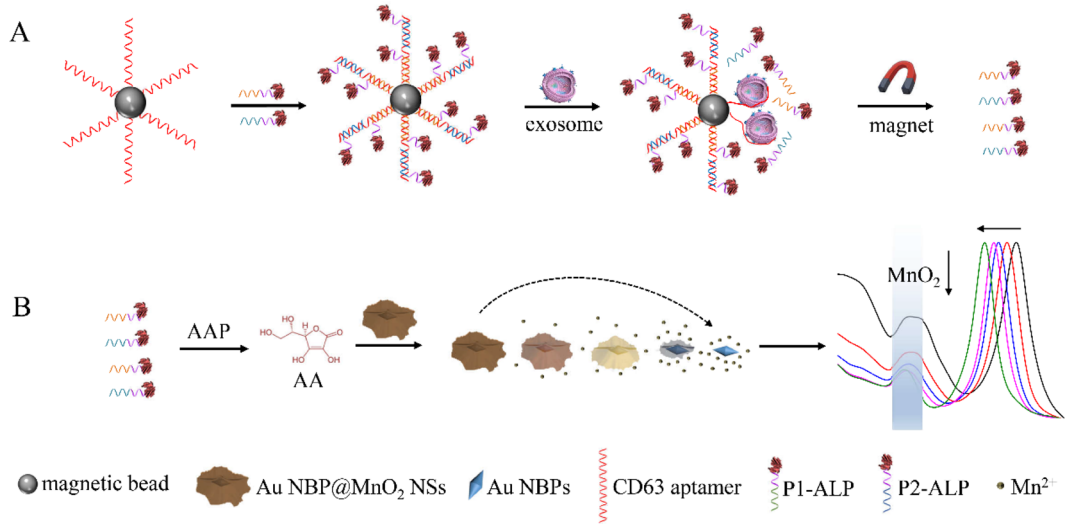

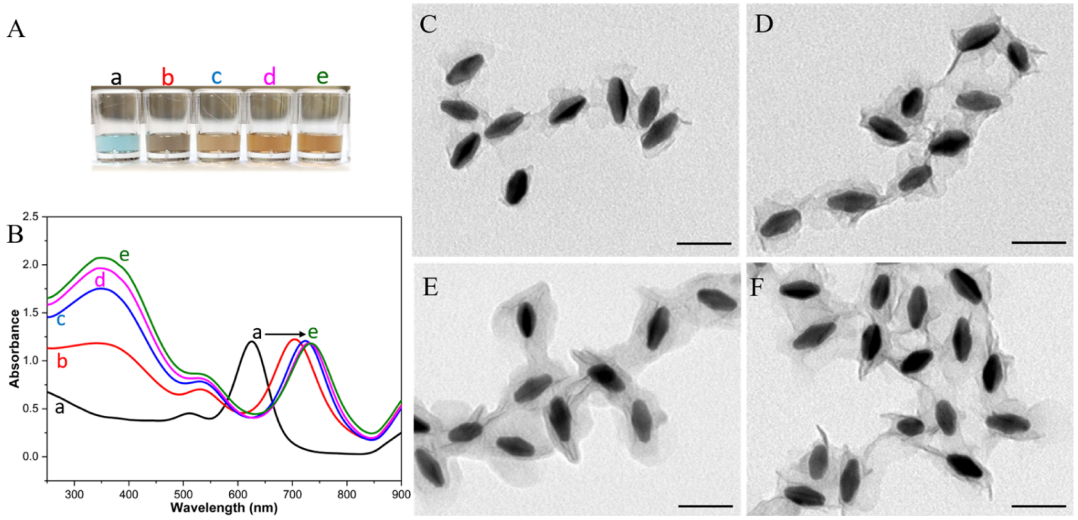

Figure 1. Characterization of low-AR Au NBP@MnO_2 NSs. (A) Photographs of the aqueous dispersions of low-AR Au NBPs@PSS and low-AR Au NBP@MnO_2 NSs: a, low-AR Au NBPs@PSS and b−e, low-AR Au NBP@MnO_2 NSs with different waist diameters (29 ± 2, 43 ± 3, 57 ± 3, and 58 ± 4 nm). (B) UV−vis spectra of the five aqueous dispersions corresponding to a−e in A. TEM images of low-AR Au NBP@MnO_2 NSs with different sizes of MnO_2 nanosheets corresponding to b−e. Scale bars represent 50 nm.

washed with PBS buffer three times, and the resulted aptamer-modified magnetic beads were redispersed in 1 mL of PBS buffer for further experiment.

Analysis of Exosomes Based on the Plasmonic Biosensor. A total of 10 μL of diverse concentrations of exosomes was separately incubated with 100 μL of aptamer-modified magnetic beads at 37 °C for 2 h. After magnetic separation, the released P1-ALP and P2-ALP were left in the supernatant and applied in the next step. Afterward, 30 μL of 5 mM L-ascorbic acid 2-phosphate (AAP) was added to the supernatant and incubated for 30 min at 37 °C. Finally, 30 μL of Au NBP@MnO_2 NSs was introduced to the above-mentioned solution. After 5 min, 30 μL of 16 mM sodium orthovanadate (Na_3VO_4) was added to inhibit the activity of ALP, and then, the UV−vis absorption spectra of the solutions were measured. Moreover, the color of the reaction system was recorded using a digital camera.

Exosomes derived from serum samples were analyzed in the same way as quantification of exosomes in buffer solutions. Additionally, serum samples were centrifuged at 10,000 g for 30 min at 4 °C prior to analysis without any other purification steps.

RESULTS AND DISCUSSION

Principle of the Plasmonic Colorimetric Biosensor for Exosome Detection. The principle of plasmonic colorimetric detection of exosomes is illustrated in Scheme 2, consisting of two major processes: exosome-induced competitive reaction and etching of Au NBP@MnO_2 NSs. As displayed in Scheme 2A, the CD63 aptamer, P1-ALP, and P2-ALP were conjugated onto magnetic beads. CD63, a sort of ubiquitous tetraspanins enriched on the surface of exosomes, was used as capture sites and triggered the competitive reaction. The presence of exosomes broke up the hybridization complex (CD63 aptamer/P1-ALP/P2-ALP) because the combination of the

https://dx.doi.org/10.1021/acs.analchem.0c04136
Anal. Chem. XXXX, XXX, XXX−XXX

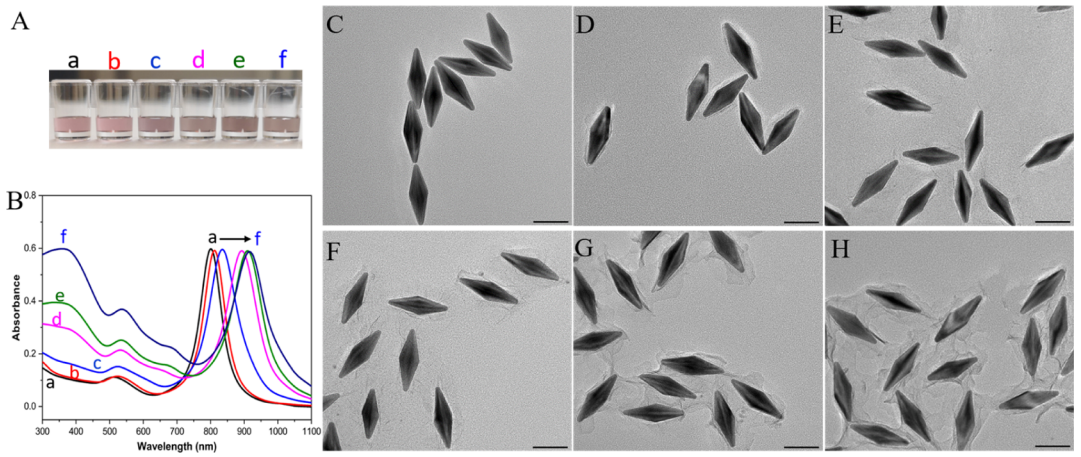

Figure 2. Characterization of large-AR Au NBP@MnO_2 NSs. (A) Photographs of the aqueous dispersions of large-AR Au NBPs@PSS and large-AR Au NBP@MnO_2 NSs: a, large-AR Au NBPs@PSS and b−f, large-AR Au NBP@MnO_2 NSs with different waist diameters (20 ± 2, 26 ± 2, 37 ± 2, 56 ± 2, and 60 ± 3 nm). (B) UV−vis spectra of the six aqueous dispersions corresponding to a−f in (A). (C−H) TEM images of large-AR Au NBP@MnO_2 NSs with different sizes of MnO_2 nanosheets corresponding to a−f. Scale bars represent 50 nm.

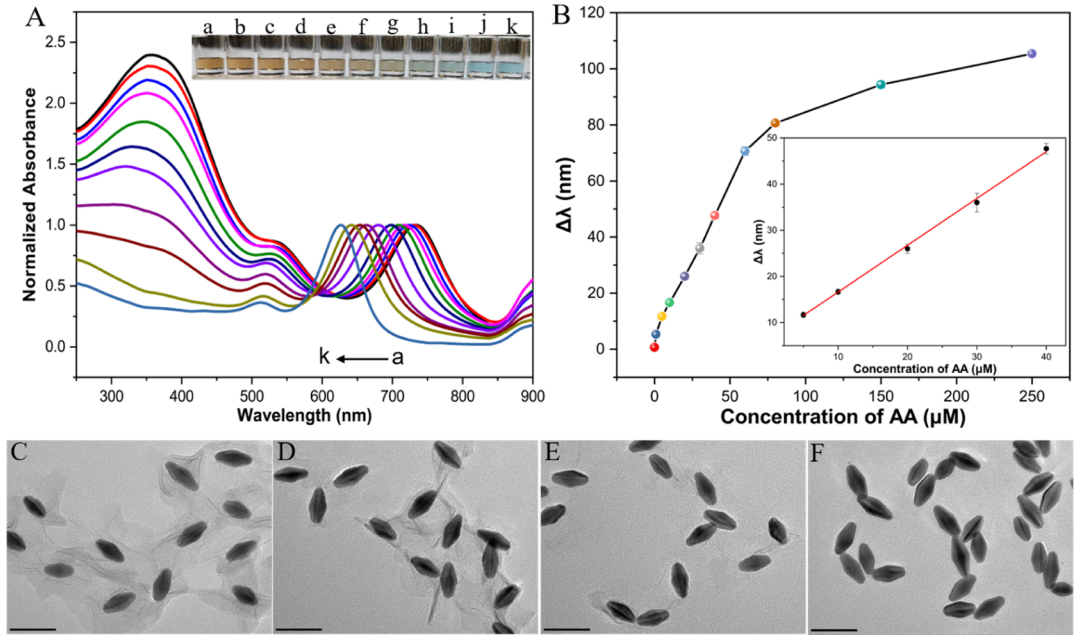

Figure 3. (A) Color variation and corresponding UV−vis absorption spectra of low-AR Au NBP@MnO_2 NSs incubated with different concentrations of AA from 0 to 250 μM. The concentrations of AA are, respectively, 0, 1.0, 5.0, 10, 20, 30, 40, 60, 80, 150, and 250 μM from a to k. (B) Plot of $\Delta\lambda$ vs concentration of AA. Inset: linear relationship between $\Delta\lambda$ and the concentration of AA from 5.0 to 40 μM. The error bars represent the standard deviation of three measurements. TEM images of low-AR Au NBP@MnO_2 NSs incubated with various AA concentrations of 0 (C), 30 (D), 80 (E), and 250 μM (F). Scale bars represent 50 nm in all images.

CD63 aptamer with CD63 is stronger than that of the CD63 aptamer with P1-ALP and P2-ALP. Thus, P1-ALP and P2-ALP were released into the supernatant. Remarkably, one exosome can make two placeholder chains release, and thus, the signal amplification can be realized by the release of double the amount of placeholder chains. Therefore, a large number of ALPs were introduced simply by the competitive reaction, resulting in the enhancement in sensitivity. As shown in Scheme 2B, the released P1-ALP and P2-ALP catalyzed the dephosphorylation of AAP to produce ascorbic acid (AA). The produced AA as a reductant etched MnO_2 nanosheets to generate Mn^{2+} and was oxidized into dehydrogenated ascorbic acid (DHA). The generated Mn^{2+} and DHA did not affect the reliability and stability of the biosensor. Meanwhile, the morphological change of Au NBP@MnO_2 NSs induced by etching contributed to the blue shift in the LSPR band of Au NBPs. Therefore, exosomes can be quantified simply and sensitively on the basis of ALP-triggered etching of Au NBP@MnO_2 NSs.

Characterization of Au NBPs and Au NBP@MnO_2 NSs. Au NBPs with different aspect ratios were synthesized by adjusting the amount of gold seeds without additional purification. For Au NBPs with a low aspect ratio (low-AR, 1.99), they have a transversal plasmon band at 512 nm and a longitudinal plasmon band at 628 nm (Figure S1A). After being modified with PSS, the electrical charges of Au NBPs were changed from +20.3 to −18.7 mV (Figure S1B). As shown in Figure S1C, the morphology of low-AR Au NBPs was

https://dx.doi.org/10.1021/acs.analchem.0c04136
Anal. Chem. XXXX, XXX, XXX−XXX

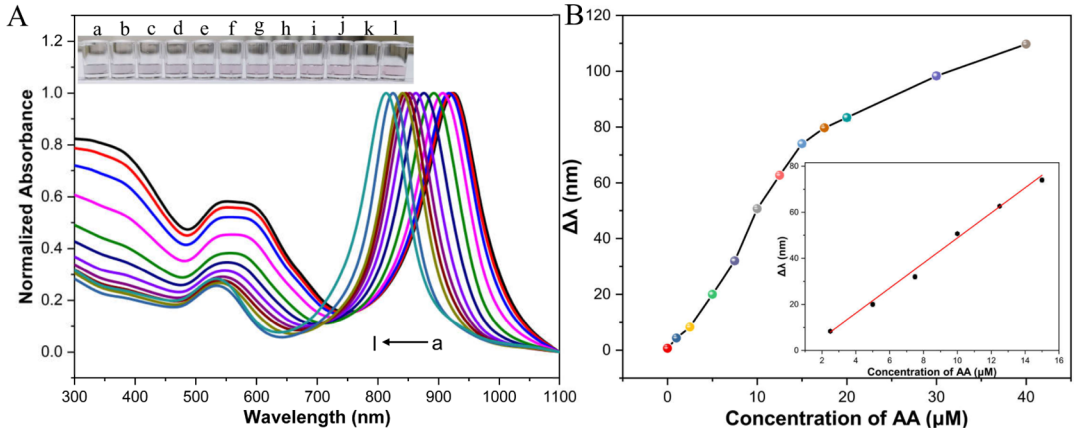

Figure 4. (A) Color variation and corresponding UV−vis absorption spectra of large-AR Au NBP@MnO_2 NSs incubated with different concentrations of AA from 0 to 40 μM. The concentrations of AA are, respectively, 0, 1.0, 2.5, 5.0, 7.5, 10, 12.5, 15, 17.5, 20, 30, and 40 μM from a to l. (B) Plot of $\Delta\lambda$ vs concentrations of AA. Inset: linear relationship between $\Delta\lambda$ and the concentration of AA from 2.5 to 15 μM. The error bars represent the standard deviation of three measurements.

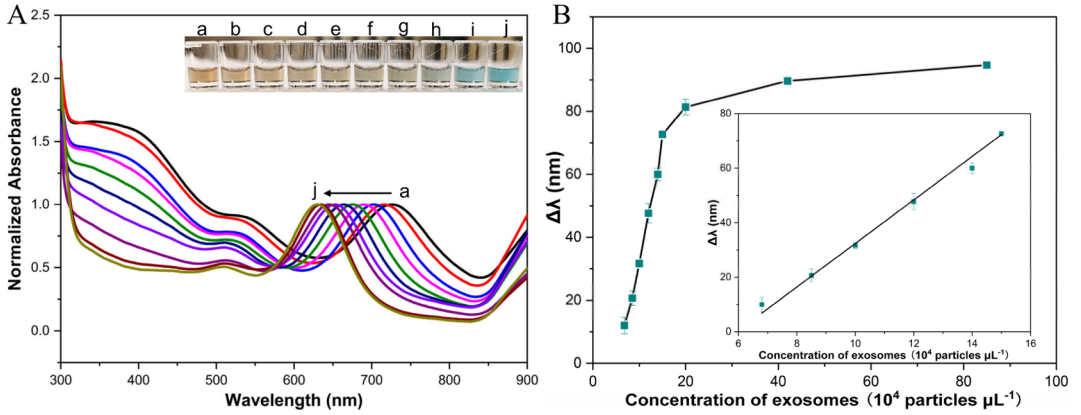

Figure 5. (A) UV−visible spectra of low-AR Au NBP@MnO_2 NSs in response to different concentrations of exosomes. The concentrations of exosomes are, respectively, 0, 6.8, 8.5, 10, 12, 14, 15, 20, 42, and 85 × 10^4 particles μL^{-1} from a to j. Inset: the corresponding color variation of the solutions. (B) Plot of $\Delta\lambda$ vs concentrations of exosomes from 0 to 8.5 × 10^5 particles μL^{-1}. Inset: linear relationship between $\Delta\lambda$ and the concentration of exosomes in the range from 6.8 × 10^4 to 1.5 × 10^5 particles μL^{-1}. The error bars represent the standard deviation of three measurements.

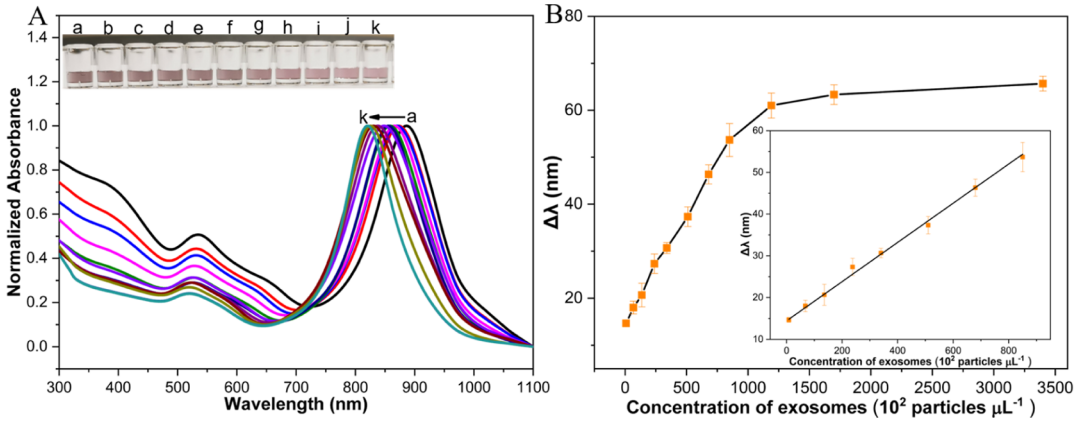

Figure 6. (A) UV−visible spectra of large-AR Au NBP@MnO_2 NSs in response to different concentrations of exosomes. The concentrations of exosomes are, respectively, 0, 8.5, 68, 136, 238, 340, 510, 680, 850, 1190, 1700, and 3400 × 10^2 particles μL^{-1} from a to k. Inset: the corresponding color variation of the solutions. (B) Plot of $\Delta\lambda$ vs concentrations of exosomes from 0 to 3.4 × 10^5 particles μL^{-1}. Inset: linear relationship between $\Delta\lambda$ and the concentration of exosomes in the range from 8.5 × 10^2 to 8.5 × 10^4 particles μL^{-1}. The error bars represent the standard deviation of three measurements.

characterized by TEM. The prepared Au NBPs have good monodispersity and uniform sizes.

The process of in situ growth of MnO_2 nanosheets on Au NBPs with different aspect ratios was monitored by both the

https://dx.doi.org/10.1021/acs.analchem.0c04136
Anal. Chem. XXXX, XXX, XXX−XXX

Table 1. Comparison of the Analytical Performance of the Current Colorimetric Methods for Exosome Detection

colorimetric substrate	linear range (particles μL^{-1})	LOD (particles μL^{-1})	ref
TMB	0.19×10^7 to 3.38×10^7	13.52×10^5	19
TMB	1.8×10^4 to 7.9×10^5	2.2×10^3	40
TMB	1.84×10^6 to 2.21×10^7	5.2×10^5	20
TMB	0.4×10^5 to 6.0×10^5	3.58×10^6	15
TMB	2.2×10^5 to 2.4×10^7	2.2×10^4	14
Au NRs	1.4×10^3 to 2.8×10^5	1.6×10^2	30
polydiacetylene liposomes	not given	3×10^5	41
1,4-phenylenediamine	1.0×10^4 to 5.0×10^5	3.40×10^3	42
low-AR Au NBP@MnO_2 NSs	6.8×10^4 to 1.5×10^5	2.20×10^3	our work
large-AR Au NBP@MnO_2 NSs	8.5×10^2 to 8.5×10^4	1.35×10^2	our work

UV−vis spectra and TEM images. The characterization of low-AR Au NBPs decorated with MnO_2 nanosheets is shown in Figure 1. During the growth of MnO_2 nanosheets, the absorbance of the characteristic peak of MnO_2 nanosheets around 360 nm got stronger with the increase in the amount of $KMnO_4$ solution. Correspondingly, the red shift of the LSPR peak of low-AR Au NBPs occurred from 630 to 730 nm, along with the plentiful multicolor variation, because the refractive index of MnO_2 nanosheets is larger than that of water. However, the LSPR peak and color of the solution no longer had significant alterations after the $KMnO_4$ solution was added three times (Figure 1A,B). The morphological transformations of low-AR Au NBP@MnO_2 NSs were further validated by TEM. Figure 1C−F exhibits TEM images of low-AR Au NBP@MnO_2 NSs with different waist diameters (29 ± 2, 43 ± 3, 57 ± 3, and 58 ± 4 nm) corresponding to the addition of $KMnO_4$ one, two, three, and four times. Au NBPs were successfully decorated with MnO_2 nanosheets, and the size of MnO_2 nanosheets obviously increased with the increased concentration of $KMnO_4$, which is consistent with the result of the UV−vis spectra.

By adjusting the amount of seed solution, we fabricated Au NBPs with a large aspect ratio (large-AR, 3.73), and the characterization of large-AR Au NBPs is exhibited in Figure 2. We also decorated MnO_2 nanosheets on large-AR Au NBPs. Compared to those of low-AR Au NBPs, the extinction spectra of large-AR Au NBPs and large-AR Au NBP@MnO_2 NSs present narrower LSPR bands (Figure 2B), indicating the higher refractive index sensitivity of large-AR Au NBP@MnO_2 NSs. The waist diameters of large-AR Au NBP@MnO_2 NSs also significantly grew from 20 ± 2 to 60 ± 3 nm, as shown in Figure 2D−H. However, the color change was not obvious during the in situ reduction of MnO_2 nanosheets on large-AR Au NBPs owing to the limited discrimination of the near-infrared region by naked eyes. From the abovementioned characterization, the proposed synthesis method can effectively avoid any self-nucleation of MnO_2, and the prepared Au NBP@MnO_2 NSs are stable in solutions with different pHs (Figure S2). Moreover, the MnO_2 nanosheets can be simply etched by the reductants, which contributes to the blue shift of Au NBPs.

Comparison of Sensitivity of Au NP@MnO_2 NSs, Au NR@MnO_2 NSs, and Au NBP@MnO_2 NSs. We used AA as a model analyte to investigate the sensitivity of Au NBP@MnO_2 NSs, Au NP@MnO_2 NSs, and Au NR@MnO_2 NSs, and the longitudinal LSPR shift ($\Delta\lambda$) was used as an indicator to evaluate the sensitivity. In order to obtain the maximum $\Delta\lambda$, we selected low-AR Au NBP@MnO_2 NSs with a waist diameter of 58 ± 4 nm and large-AR Au NBP@MnO_2 NSs with a waist diameter of 60 ± 3 nm for subsequent experiments. Various concentrations of AA were incubated with Au NBP@MnO_2 NSs, and the UV−vis absorption spectra were employed to monitor the etching degree of Au NBP@MnO_2 NSs by AA. As shown in Figure 3A, the longitudinal LSPR peak of low-AR Au NBPs shifts from 730 to 630 nm. Meanwhile, the color varies from yellowish brown to brown, gray-brown, gray-green, and blue. As shown in Figure 3B, the decrease in $\Delta\lambda$ of Au NBPs shows positive correlation with the increase in AA concentration (0−250 μM). A linear dependence between the $\Delta\lambda$ and the concentration of AA from 5.0 to

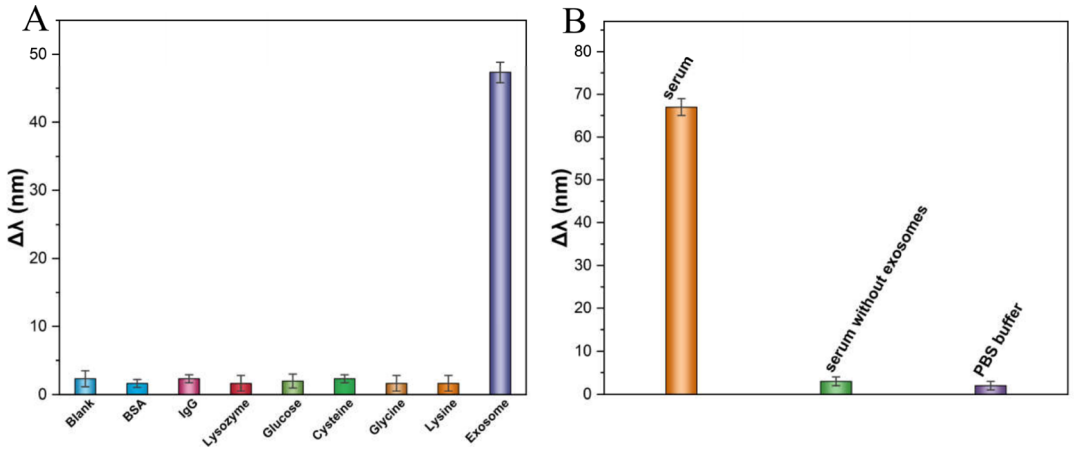

Figure 7. Specificity of the plasmonic colorimetric biosensor toward exosome. (A) $\Delta\lambda$ of exosomes (6.8×10^4 particles μL^{-1}), BSA (100 μg mL^{-1}), IgG (100 μg mL^{-1}), lysozyme (100 μg mL^{-1}), glucose (10 mM), cysteine (10 mM), glycine (10 mM), and lysine (10 mM). (B) $\Delta\lambda$ of large-AR Au NBP@MnO_2 NSs toward the serum samples and controls (serum samples without exosomes and the PBS buffer). The error bars represent the standard deviation of three measurements.

https://dx.doi.org/10.1021/acs.analchem.0c04136
Anal. Chem. XXXX, XXX, XXX−XXX

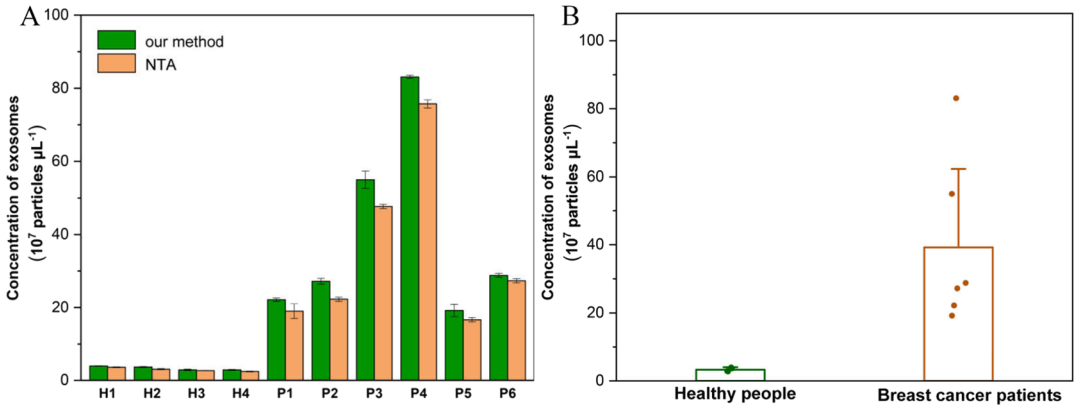

Figure 8. (A) Quantification of exosomes in serum samples from four healthy people (H1−H4) and six breast cancer patients (P1−P6) by our method and NTA. (B) Boxplots of exosome concentrations from 10 human subjects measured by our method. The error bars represent the standard deviation of three measurements.

40 μM was realized. The limit of detection (LOD) for AA was estimated as 1.71 μM. The morphological change of low-AR Au NBP@MnO_2 NSs was inspected by TEM (Figure 3C−F). TEM images demonstrate that MnO_2 nanosheets were gradually etched with the concentration of AA increasing, which contributes to the shift of the longitudinal LSPR peak of Au NBPs. The etching degree of large-AR Au NBP@MnO_2 NSs by AA is exhibited in Figure 4. There is a shift of the LSPR peak from 925 to 815 nm with less-obvious color transition (Figure 4A), and there is a linear relationship between $\Delta\lambda$ and AA concentration from 2.5 to 15 μM with a LOD of 0.31 μM (Figure 4B).

We also inspected the sensitivity of AuNP@MnO_2 NSs (Figure S4) and Au NR@MnO_2 NSs (Figure S5). The aspect ratio of Au NRs is similar to that of large-AR Au NBPs. It is more sensitive employing Au NBP@MnO_2 NSs as substrates than employing AuNP@MnO_2 NSs (LOD = 8.50 μM for AA) or Au NR@MnO_2 NSs (LOD = 5.56 μM for AA) as substrates. The enhanced sensitivity of Au NBP@MnO_2 NSs is due to their sharper apexes. Furthermore, the large-AR Au NBP@MnO_2 NSs have better sensitivity at lower target concentrations than low-AR Au NBP@MnO_2 NSs, which can be ascribed to the higher molar extinction coefficient and narrower LSPR band width of large-AR Au NBPs.

Feasibility of the Proposed Method for Exosome Detection. On the basis of the abovementioned work, we investigated the feasibility of exosome detection employing Au NBP@MnO_2 NSs as substrates. First, we conducted ALP-induced etching of low-AR Au NBP@MnO_2 NSs (Figure S6A,B). The color change of the solution occurred in the presence of Au NBP@MnO_2 NSs, AAP, and ALP, which is similar to the reaction between Au NBP@MnO_2 NSs and AA. However, the color of solutions remained unchanged in the absence of AAP or ALP. This is because ALP triggered the hydrolysis of AAP to generate AA. These results suggest that the etching of Au NBP@MnO_2 NSs induced by ALP is feasible. Afterward, the feasibility of exosome-induced competitive reaction was validated through PAGE analysis, as displayed in Figure S6C. Lanes 1−3, respectively, exhibit bands of the CD63 aptamer, P1, and P2. After incubation of the CD63 aptamer with P1 and P2, a new band (lane 4) was observed, indicating the hybridization of the three DNA chains. After exosomes were introduced, a clear band (lane 5) with a much lower migration than the band in the lane 4 presented, showing that the competitive reaction was successfully triggered by exosomes. Finally, exosomes were introduced into the reaction system to trigger competitive reaction, and then, Au NBP@MnO_2 NSs were etched. As shown in Figure S6D, an obvious shift of longitudinal LSPR of Au NBPs from 730 to 630 nm was observed in the presence of exosomes with a concentration of 1.7×10^6 particles μL^{-1}. Correspondingly, color variation from brown to blue was easily distinguished. Thus, these results validate that the proposed principle is feasible for exosome detection.

Optimization of Experimental Conditions. Some main experimental conditions of exosome detection were optimized, including the concentrations of P1 and P2, hydrolysis time, and etching time. The concentrations of P1 and P2 were investigated for ensuring the effectiveness of the exosome-induced competitive reaction. In order to achieve the signal amplification via replacement of P1 and P2 by exosomes, the P1 and P2 hybridized with the CD63 aptamer must be excessive. We used FAM instead of ALP to label P1 (P1-FAM) and P2 (P2-FAM) and collected the fluorescence spectra of the supernatant after hybridization. The fluorescence intensity increased obviously with the concentration ratio of P1-FAM/P2-FAM and magnetic beads increasing from 0 to 20 μmol g^{-1} and then reached a plateau with a ratio higher than 12.5 μmol g^{-1} (Figure S7A). Therefore, 12.5 μmol g^{-1} was chosen for further experiments. The effects of hydrolysis time of AAP and time of the etching reaction on $\Delta\lambda$ were also studied, and 35 and 5 min were selected as hydrolysis time and etching time, respectively (Figure S7B,C).

Detection of Exosomes Using the Proposed Plasmonic Colorimetric Biosensor. Exosomes were extracted from human breast carcinoma cells (MCF-7) using the standard ultracentrifugation method with a little modification according to the literature.[39] Under the optimal conditions, exosomes were detected employing low-AR and large-AR Au NBP@MnO_2 NSs as substrates. For low-AR Au NBP@MnO_2 NSs, multicolor conversion from yellowish brown, brown, gray-brown, gray-green, and green to blue presents with the concentration of exosomes increasing from 0 to 8.5×10^5 particles μL^{-1} in inset of Figure 5A. At the same time, the longitudinal LSPR band of Au NBPs blue-shifted (Figure 5). Additionally, there is a linear relationship (inset of Figure 5B) between $\Delta\lambda$ and the concentration of exosomes from 6.8×10^4 to 1.5×10^5 particles μL^{-1}, fitted as $y = 7.9x - 46$ (where y and x represent the $\Delta\lambda$ and the concentration of exosomes, respectively). The LOD was calculated as 2.2×10^3 particles

https://dx.doi.org/10.1021/acs.analchem.0c04136
Anal. Chem. XXXX, XXX, XXX−XXX

μL^{-1} according to $3\sigma/K$ (σ represents the standard deviation of the control group without exosomes and K is the slope of the standard curve). Additionally, the relative standard deviations (RSDs) were 1.3−6.9% employing low-AR Au NBP@MnO_2 NSs as substrates. A multicolor visual detection of exosomes was realized using the low-AR Au NBP@MnO_2 NSs as polychromatic substrates. For large-AR Au NBP@MnO_2 NSs, a linear relationship is displayed between $\Delta\lambda$ and the concentration of exosomes from 8.5×10^2 to 8.5×10^4 particles μL^{-1} with RSDs of 3.8−7.7%, as shown in Figure 6. The LOD for exosomes is 1.35×10^2 particles μL^{-1}, which is more sensitive than that of all of the reported colorimetric assays (Table 1). The low LOD is attributed to the enhanced sensitivity caused by the signal amplification and the excellent refractive index sensitivity of Au NBPs.

Selectivity of the Proposed Plasmonic Colorimetric Biosensor. Specificity is a pivotal criterion to evaluate the anti-interference ability of biosensors. In order to evaluate the specificity of the biosensor, effects of some possible interfering substances in serum samples, such as BSA, IgG, lysozyme, glucose, cysteine, glycine, and lysine, were investigated. Figure 7A clearly shows that the $\Delta\lambda$ values ascribed to these interfering substances are negligible compared to the obvious $\Delta\lambda$ for exosomes. Furthermore, the effects of the serum samples and the serum samples without exosomes and the PBS buffer were also inspected. As displayed in Figure 7B, the serum samples show much larger $\Delta\lambda$ than the serum samples without exosomes and the PBS buffer. Meanwhile, the $\Delta\lambda$ of the serum samples without exosomes is almost the same as that of the PBS buffer. Therefore, these results prove the good specificity of the proposed plasmonic biosensor for exosome assay.

Application of the Proposed Method in Real Sample Assay. Different levels of exosome expression are related to the patients' condition. In order to evaluate the practical application of the proposed plasmonic colorimetric detection method, exosomes in serums from healthy people and breast cancer patients were analyzed (Figure 8A). As a control, exosomes derived from 10 human serum samples were extracted according to the procedures of ultracentrifugation in the Supporting Information and measured by nanoparticle tracking analysis (Particle Metrix, Meerbusch, Germany). Compared with NTA, our method has obvious advantages in real sample assay for it does not require complicated processing steps. The experiments were approved by the Ethics Committee of Academic Advisory Board, Northeastern University, China, and the institutional committee of human experimentation of Northeastern University Hospital. As shown in Figure 8B, the average concentration of exosomes from breast cancer patients is significantly higher (8.6-fold) than that from healthy volunteers. These preliminary results indicate that our method has a promising application perspective.

CONCLUSIONS

A highly sensitive and easy-to-operate plasmonic colorimetric method was successfully developed for exosome detection. The introduction of ALP via competitive reaction efficiently amplified the signal in a simple way, and the utilization of Au NBP@MnO_2 NSs with captivating optical properties as substrates greatly enhanced the sensitivity. Owing to the abovementioned merits, our method exhibits satisfactory sensitivity down to 1.35×10^2 particles μL^{-1} for exosomes. Moreover, this method was used for the analysis of human serum samples and shows good accuracy and great potential for exosome-based cancer diagnosis. This plasmonic colorimetric strategy may be applied for specific detection toward a targeted exosome population and extended to detect other biomolecules by changing the capture sequences..

ASSOCIATED CONTENT

Supporting Information

The Supporting Information is available free of charge at https://pubs.acs.org/doi/10.1021/acs.analchem.0c04136.

Materials; preparation of Au NBPs; purification of exosomes; characterization of synthesized low-AR Au NBPs and low-AR Au NBPs@PSS; stability testing of Au NBP@MnO_2 NSs at different pHs for 60 min incubation; optimization of reaction pH between AA and Au NBP@MnO_2 NSs; detection of AA using AuNP@MnO_2 NSs; detection of AA using Au NR@MnO_2 NSs; feasibility of the detection strategy; optimization of experimental conditions; investigation of the effects of etching time, temperature, and temperature/humidity; table of sequences of oligonucleotides used in this work; and table of experimental conditions for evaluating the effects of temperature and humidity during a week (PDF)

AUTHOR INFORMATION

Corresponding Authors

Zhangrun Xu − *Research Center for Analytical Sciences, Northeastern University, Shenyang 110819, P. R. China*; orcid.org/0000-0003-3834-1145; Email: xuzr@mail.neu.edu.cn

Chunguang Yang − *Research Center for Analytical Sciences, Northeastern University, Shenyang 110819, P. R. China*; Email: yangcg@mail.neu.edu.cn

Authors

Yingzhi Zhang − *Research Center for Analytical Sciences, Northeastern University, Shenyang 110819, P. R. China*

Junye Jiao − *Research Center for Analytical Sciences, Northeastern University, Shenyang 110819, P. R. China*

Yunyun Wei − *Research Center for Analytical Sciences, Northeastern University, Shenyang 110819, P. R. China*

Danni Wang − *Research Center for Analytical Sciences, Northeastern University, Shenyang 110819, P. R. China*

Complete contact information is available at: https://pubs.acs.org/10.1021/acs.analchem.0c04136

Notes

The authors declare no competing financial interest.

ACKNOWLEDGMENTS

This work was supported by the National Natural Science Foundation of China (21874015 and 21675020). We particularly appreciate professor Jin Fang and her group at the Department of Cell Biology, China Medical University for purification of exosomes. Special thanks are due to the instrumental and data analysis from Analytical and Testing Center, Northeastern University.

REFERENCES

(1) Raposo, G.; Stoorvogel, W. *J. Cell Biol.* **2013**, *200*, 373−383.

(2) Kumar, S.; Michael, I. J.; Park, J.; Granick, S.; Cho, Y.-K. *Small* **2018**, *14*, 1802052−1802058.
(3) Jeppesen, D. K.; Fenix, A. M.; Franklin, J. L.; Higginbotham, J. N.; Zhang, Q.; Zimmerman, L. J.; Liebler, D. C.; Ping, J.; Liu, Q.; Evans, R.; Fissell, W. H.; Patton, J. G.; Rome, L. H.; Burnette, D. T.; Coffey, R. J. *Cell* **2019**, *177*, 428−445.
(4) Greening, D. W.; Gopal, S. K.; Xu, R.; Simpson, R. J.; Chen, W. *Semin. Cell Dev. Biol.* **2015**, *40*, 72−81.
(5) Zhang, W.; Xia, W.; Lv, Z.; Ni, C.; Xin, Y.; Yang, L. *Cell. Physiol. Biochem.* **2017**, *41*, 755−768.
(6) Pegtel, D. M.; Gould, S. J. *Annu. Rev. Biochem.* **2019**, *88*, 487−514.
(7) Cui, S.; Cheng, Z.; Qin, W.; Jiang, L. *Lung Canc.* **2018**, *116*, 46−54.
(8) Ghosh, R. K.; Pandey, T.; Dey, P. *Cytopathology* **2019**, *30*, 138−143.
(9) Coumans, F. A. W.; Doggen, C. J. M.; Attard, G.; de Bono, J. S.; Terstappen, L. W. M. M. *Ann. Oncol.* **2010**, *21*, 1851−1857.
(10) Xu, H.; Liao, C.; Zuo, P.; Liu, Z.; Ye, B.-C. *Anal. Chem.* **2018**, *90*, 13451−13458.
(11) An, Y.; Jin, T.; Zhu, Y.; Zhang, F.; He, P. *Biosens. Bioelectron.* **2019**, *142*, 111503−111509.
(12) Zhang, P.; He, M.; Zeng, Y. *Lab Chip* **2016**, *16*, 3033−3042.
(13) Wang, L.; Pan, Y.; Liu, Y.; Sun, Z.; Huang, Y.; Li, J.; Yang, J.; Xiang, Y.; Li, G. *ACS Appl. Mater. Interfaces* **2020**, *12*, 322−329.
(14) Chen, Z.; Cheng, S.-B.; Cao, P.; Qiu, Q.-F.; Chen, Y.; Xie, M.; Xu, Y.; Huang, W.-H. *Biosens. Bioelectron.* **2018**, *122*, 211−216.
(15) Chen, J.; Xu, Y.; Lu, Y.; Xing, W. *Anal. Chem.* **2018**, *90*, 14207−14215.
(16) Shin, H.; Jeong, H.; Park, J.; Hong, S.; Choi, Y. *ACS Sens.* **2018**, *3*, 2637−2643.
(17) Zhang, X.; Liu, C.; Pei, Y.; Song, W.; Zhang, S. *ACS Appl. Mater. Interfaces* **2019**, *11*, 28671−28680.
(18) Stremersch, S.; Marro, M.; Pinchasik, B.-E.; Baatsen, P.; Hendrix, A.; De Smedt, S. C.; Loza-Alvarez, P.; Skirtach, A. G.; Raemdonck, K.; Braeckmans, K. *Small* **2016**, *12*, 3292−3301.
(19) Wang, Y.-M.; Liu, J.-W.; Adkins, G. B.; Shen, W.; Trinh, M. P.; Duan, L.-Y.; Jiang, J.-H.; Zhong, W. *Anal. Chem.* **2017**, *89*, 12327−12333.
(20) Xia, Y.; Liu, M.; Wang, L.; Yan, A.; He, W.; Chen, M.; Lan, J.; Xu, J.; Guan, L.; Chen, J. *Biosens. Bioelectron.* **2017**, *92*, 8−15.
(21) Zhang, Y.; Guo, Y.; Xianyu, Y.; Chen, W.; Zhao, Y.; Jiang, X. *Adv. Mater.* **2013**, *25*, 3802−3819.
(22) Howes, P. D.; Rana, S.; Stevens, M. M. *Chem. Soc. Rev.* **2014**, *43*, 3835−3853.
(23) Zheng, W.; Jiang, X. *Analyst* **2016**, *141*, 1196−1208.
(24) Choi, Y.; Hwang, J. H.; Lee, S. Y. *Small Methods* **2018**, *2*, 1700351−1700359.
(25) Tang, L.; Li, J. *ACS Sens.* **2017**, *2*, 857−875.
(26) Ma, F.; Zhang, Q.; Zhang, C.-y. *J. Mater. Chem. B* **2020**, *8*, 3488−3501.
(27) Wang, D.; Zhang, Y.; Zhao, X.; Xu, Z. *Sens. Actuators, B* **2019**, *296*, 126646−126653.
(28) Yang, X.; Gao, Z. *Chem. Commun.* **2015**, *51*, 6928−6931.
(29) Qi, Y.; Zhao, J.; Weng, G.-j.; Li, J.-j.; Li, X.; Zhu, J.; Zhao, J.-w. *J. Mater. Chem. C* **2018**, *6*, 12283−12293.
(30) Zhang, Y.; Wang, D.; Yue, S.; Lu, Y.; Yang, C.; Fang, J.; Xu, Z. *ACS Sens.* **2019**, *4*, 3210−3218.
(31) Chen, H.; Shao, L.; Li, Q.; Wang, J. *Chem. Soc. Rev.* **2013**, *42*, 2679−2724.
(32) Li, Q.; Zhuo, X.; Li, S.; Ruan, Q.; Xu, Q.-H.; Wang, J. *Adv. Opt. Mater.* **2015**, *3*, 801−812.
(33) Lee, S.; Mayer, K. M.; Hafner, J. H. *Anal. Chem.* **2009**, *81*, 4450−4455.
(34) Guo, Y.; Zhu, X.; Li, N.; Yang, J.; Yang, Z.; Wang, J.; Yang, B. *J. Phys. Chem. C* **2019**, *123*, 7336−7346.
(35) Xu, S.; Jiang, L.; Nie, Y.; Wang, J.; Li, H.; Liu, Y.; Wang, W.; Xu, G.; Luo, X. *ACS Appl. Mater. Interfaces* **2018**, *10*, 26851−26858.
(36) Xu, S.; Ouyang, W.; Xie, P.; Lin, Y.; Qiu, B.; Lin, Z.; Chen, G.; Guo, L. *Anal. Chem.* **2017**, *89*, 1617−1623.
(37) Chateau, D.; Liotta, A.; Vadcard, F.; Navarro, J. R. G.; Chaput, F.; Lermé, J.; Lerouge, F.; Parola, S. *Nanoscale* **2015**, *7*, 1934−1943.
(38) Ling, Y.; Zhang, D.; Cui, X.; Wei, M.; Zhang, T.; Wang, J.; Xiao, L.; Xia, Y. *Angew. Chem., Int. Ed.* **2019**, *58*, 10542−10546.
(39) Théry, C.; Amigorena, S.; Raposo, G.; Clayton, A. *Curr. Protoc. Cell Biol.* **2006**, *30*, 3.22.1.
(40) He, F.; Liu, H.; Guo, X.; Yin, B.-C.; Ye, B.-C. *Anal. Chem.* **2017**, *89*, 12968−12975.
(41) Kim, C.; Lee, K. *Biomacromolecules* **2019**, *20*, 3392−3398.
(42) Xia, Y.; Chen, T.; Chen, G.; Weng, Y.; Zeng, L.; Liao, Y.; Chen, W.; Lan, J.; Zhang, J.; Chen, J. *Talanta* **2020**, *214*, 120851−120860.

https://dx.doi.org/10.1021/acs.analchem.0c04136
Anal. Chem. XXXX, XXX, XXX−XXX